Quiet time equatorial mass density distribution derived from AMPTE/CCE and GOES using the magnetoseismology technique

Kyungguk Min,[1] Jacob Bortnik,[1,2] Richard E. Denton,[3] Kazue Takahashi,[4] Jeongwoo Lee,[1,5] and Howard J. Singer[6]

Received 8 May 2013; revised 26 August 2013; accepted 10 September 2013; published 3 October 2013.

[1] An inversion technique for estimating the properties of the magnetospheric plasma from the harmonic frequencies of the toroidal standing Alfvén waves has been used to derive the global equatorial mass density covering radial distances from 4 to 9 Earth radii (R_E), within the local time sector spanning from 0300 to 1900 h. This broad range of L shell extending to the outer magnetosphere allows us to examine the local time and radial dependence of the quiet time equatorial mass density during solar minimum and thereby construct a global distribution of the equatorial mass density. The toroidal Alfvén waves were detected with magnetometers on the Active Magnetospheric Particle Tracer Explorers (AMPTE)/Charge Composition Explorer (CCE) during the nearly 5 year interval from August 1984 to January 1989 and on the Geostationary Operational Environmental Satellites (GOES) (10, 11, and 12) for 2 years from 2007 to 2008, both of which were operating during solar minimum years. The derived equatorial mass density, ρ_{eq}, at geosynchronous orbit (GEO) monotonically increases with increasing magnetic local time (MLT) from the nightside toward the dusk sector. At other radial distances, ρ_{eq} has the same MLT variation as that of GEO, while the magnitude logarithmically decreases with increasing L value. An investigation of the *Dst* and *Kp* dependence shows that the median value of ρ_{eq} varies little in the daytime sector during moderately disturbed times, which agrees with previous studies. ρ_{eq} calculated from the $F_{10.7}$ dependent empirical model shows good agreement with that of CCE but overestimates that of GOES probably due to the extreme solar cycle minimum in years 2007–2008.

Citation: Min, K., J. Bortnik, R. E. Denton, K. Takahashi, J. Lee, and H. J. Singer (2013), Quiet time equatorial mass density distribution derived from AMPTE/CCE and GOES using the magnetoseismology technique, *J. Geophys. Res. Space Physics*, *118*, 6090–6105, doi:10.1002/jgra.50563.

1. Introduction

[2] Toroidal mode standing Alfvén waves (referred to as toroidal waves hereafter) can be used to infer the physical properties of the magnetospheric plasma that sustains the oscillation. The inversion technique, termed "normal mode magnetospheric seismology," has been used by numerous authors to derive the mass variation along the field line from space (e.g., review and references in *Denton* [2006], and recent studies by *Denton et al.* [2009], *Takahashi and Denton* [2007], and *Takahashi et al.* [2008, 2010]) to the ground (e.g., review in *Waters et al.* [2006], and references therein). Despite the limited number of toroidal frequencies observable from instruments, the strong dependence of the inversion on the accuracy of the measured frequencies and the simplified magnetic field models that made the technique difficult to deploy [*Denton et al.*, 2001, 2004a; *Takahashi et al.*, 2006], the unique advantage of remotely diagnosing the mass variation along the field line has motivated studies that led to improvements over time.

[3] We summarize only a few results from recent studies in the context of space observation. First, using a more general polynomial density model has revealed small-scale structures in the mass variation along the field line, which the simple power law variation, used traditionally, could not discern. For instance, *Takahashi et al.* [2004, 2006] and *Denton et al.* [2006] used the toroidal frequencies observed by the Combined Release and Radiation Effects Satellite (CRRES) to show the existence of a local density enhancement at the magnetic equator and that the enhancement increases with increasing radial distance. Similarly, *Takahashi and Denton* [2007] used the toroidal frequencies observed by

[1]Department of Physics, Auburn University, Auburn, Alabama, USA.
[2]Department of Atmospheric and Oceanic Sciences, University of California, Los Angeles, California, USA.
[3]Department of Physics and Astronomy, Dartmouth College, Hanover, New Hampshire, USA.
[4]Johns Hopkins University Applied Physics Laboratory, Laurel, Maryland, USA.
[5]School of Space Research, Kyung Hee University, Yongin, Korea.
[6]Space Weather Prediction Center, NOAA, Boulder, Colorado, USA.

Corresponding author: K. Min, Department of Physics, Auburn University, Auburn, AL 36849, USA. (kmin@auburn.edu)

2169-9380/13/10.1002/jgra.50563

Geostationary Operational Environmental Satellites (GOES) and found that the local enhancement is also dependent on the local time (magnetic local time (MLT)) of observation. The power law model $\rho = \rho_{eq}(LR_E/R)^{\alpha}$, used in previous studies [e.g., *Cummings et al.*, 1969], fails to capture the local maximum. Several physical mechanisms have been suggested for this local enhancement, including an enhanced potential well at the higher radial distances due to the centrifugal force [*Denton et al.*, 2006], the formation of a localized partial ring current related to the heavy ion (or oxygen) torus [*Roberts et al.*, 1987; *Takahashi and Denton*, 2007], or an anisotropic distribution (through local adiabatic processes, global transportation, or perpendicular heating by ion cyclotron waves) of the ions, or any combination thereof [*Takahashi and Denton*, 2007].

[4] The second point we highlight is the fact that the derived mass density imposes a constraint on the ion composition which is otherwise difficult to measure due mainly to the limited instrument sensitivity at low thermal speeds. *Takahashi et al.* [2006] investigated the average ion mass, a ratio of the mass density to the electron number density, to narrow down the bounds of the ion composition, and *Takahashi et al.* [2008] inferred the dominance of heavy ions in the plasma trough between the plasmasphere and drainage plume through a similar technique. *Berube et al.* [2005], on the other hand, used ground-based ULF wave diagnostics to show the enhancement of the heavy ion concentrations and the presence of a heavy ion torus during disturbed times.

[5] As a final note, *Takahashi et al.* [2010] recently reported the long-term mass density modulation by $F_{10.7}$ and sunspot number as well as short-term variation with respect to the geomagnetic indices. They showed that $F_{10.7}$ and 27 day averaged mass density are highly correlated, implying that the solar UV/EUV control of ion production at ionospheric heights is strongly reflected in mass density variations, whereas the correlation with the geomagnetic indices is somewhat weaker, although the magnetospheric convection system still controls the transport.

[6] Despite a few decades of spaceborne observations, our current understanding of the mass variation on a global scale is yet to be quantified. To this end, the current paper attempts to investigate the mass variation on a larger spatial scale than in previous studies using a large number of samples of the toroidal frequencies observed by the magnetometer on the Active Magnetospheric Particle Tracer Explorers/Charge Composition Explorer spacecraft (referred to as CCE hereafter). Along similar lines, *Takahashi et al.* [2002] used the fundamental mode frequency, f_{T1}, determined using the energetic particle as well as magnetometer data, but mainly focused on the frequency identification and indirect derivation of the mass density using the Global Core Plasma Model (GCPM) [*Gallagher et al.*, 2000]. Unlike their study, we only use the magnetometer data and use the third harmonic frequency, f_{T3}, to derive the equatorial mass density assuming a power law variation, following similar analyses by *Takahashi and Denton* [2007] and *Takahashi et al.* [2010]. We also use the GOES magnetometer data to enhance our data set and for the added purpose of cross comparison and validation of our analysis.

[7] The present paper extensively uses the results of *Takahashi et al.* [2010] for validation of our analysis procedure and intercomparison of our results. After a short description of the inversion technique in section 2, we demonstrate the identification process of the toroidal waves and the harmonics with a sample orbit in section 3 and show the statistical results in detail in sections 4 and 5. We discuss and summarize the results in sections 6 and 7, respectively.

2. Normal Mode Magnetospheric Seismology

[8] The frequencies of the toroidal standing Alfvén waves depend on the field line distribution of mass, analogous to the oscillation of a string whose ends are fixed. Under the assumption of a realistic magnetic field model and axisymmetry of the equilibrium and wave perturbation in the inner magnetosphere [*Denton et al.*, 2001], the MHD shear Alfvén waves can be described by the wave equation [*Singer et al.*, 1981] (refer to typographical correction in *Denton et al.* [2004a])

$$\frac{\partial^2}{\partial s^2}\xi' + \frac{1}{h_\alpha^2 B_0}\frac{\partial}{\partial s}(h_\alpha^2 B_0)\frac{\partial}{\partial s}\xi' + \frac{\omega^2}{V_A^2}\xi' = 0, \tag{1}$$

where ξ' is the linear displacement in the direction of the oscillation $\boldsymbol{\alpha}$ (assumed to be in the azimuthal direction at the magnetic equator for the toroidal mode) divided by scale factor h_α (proportional to the distance to an adjacent field line in the direction of oscillation), V_A is the Alfvén speed, B_0 is the magnitude of the equilibrium magnetic field, and s is the distance along the field line. This wave equation can be solved in a nondipolar magnetic field geometry to obtain harmonic frequencies, ω. In this paper, we assume that the ionosphere is a perfect conductor located at radial distance 1.015 R_E ($\sim$ 100 km in altitude) [*Denton et al.*, 2006]. The Tsyganenko 89 (T89) [*Tsyganenko*, 1987, 1989] magnetic field model was used because this model only requires the *Kp* index as an input parameter. The dipole magnetic field was also used in parallel for the purpose of verification although the result is not shown in this paper.

[9] In order to derive the equatorial mass distribution from the observed toroidal harmonics, we assume the power law mass density model [*Denton et al.*, 2001, 2004a]

$$\rho = \rho_{eq}\left(\frac{LR_E}{R}\right)^{\alpha}, \tag{2}$$

where L is the farthest radial distance of the field line, R is the distance at any given point on the field line, and α is the power law index. Given this density model, the free parameters, ρ_{eq} and α, can be found by minimizing the difference between the observed toroidal frequencies and the solutions of equation (1) in a least squares sense [*Denton et al.*, 2001, 2004a].

[10] The power law index, α, is usually assumed to vary between 0 and 6 depending on the location [*Cummings et al.*, 1969]. Theoretical studies suggest that for $L < 6$ (plasmasphere), $\alpha = 0 - 1$ based on a diffusive equilibrium model and for $L > 6$ (plasmatrough), $\alpha \sim 3$–4 based on a collisional distribution model [*Lemaire and Gringauz*, 1998]. As discussed by *Takahashi et al.* [2006], equation (2) does not represent the mass variation along the field line for $L > 6$ because of the local maximum around the equator. Nevertheless, $\alpha \approx 1$ represents the mass density near the magnetic equator better than $\alpha \approx 4$ [*Takahashi et al.*, 2004; *Denton et al.*, 2006]. Following the statistical study by *Takahashi et al.* [2010], we chose $\alpha = 1$ and calculated

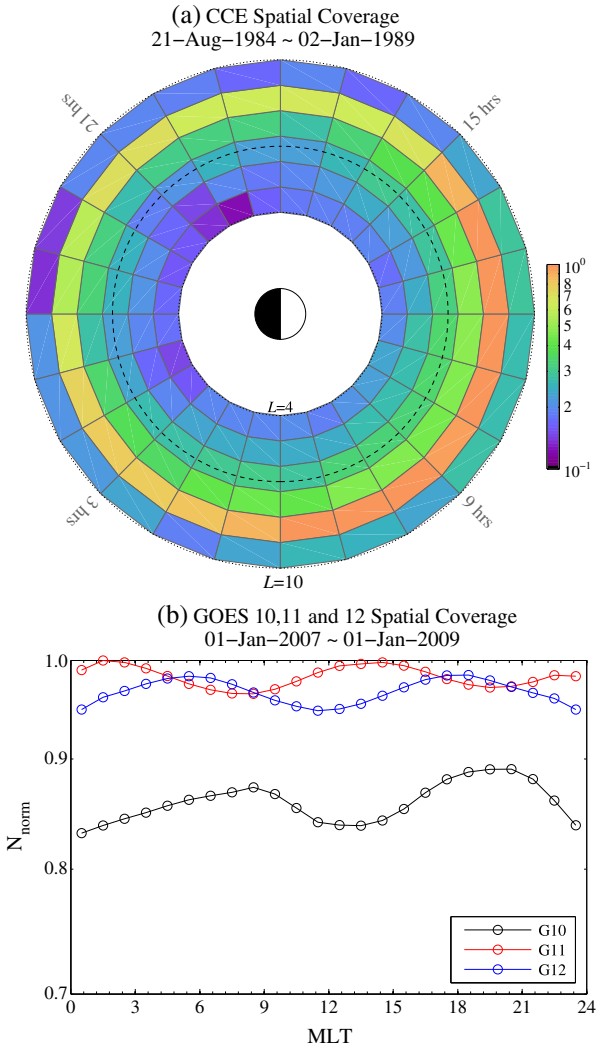

Figure 1. Spatial coverage of (a) CCE and (b) GOES intervals used in this study. The bin size is 1 R_E in radial distance (CCE only) and 1 h in MLT. The number of available field vectors in each bin is normalized to the maximum number of field vectors across all L (CCE only) and MLT bins.

ρ_{eq} to derive the global equatorial mass density distribution. In section 6.3, we revisit this assumption and discuss the effective α values.

3. Data Set and Analysis

3.1. CCE

[11] CCE acquired scientific data from August 1984 to January 1989. It had a 1.2 × 8.8 R_E elliptical orbit with an inclination of 5°. The spacecraft was spin stabilized with a spin period of 5.9 s and a spin axis that remained within 15° of the Sun-Earth line. As shown in Figure 1a, CCE covered the near-equatorial plane over a wide range of L values although the number of samples are biased toward the prenoon sector. The large number of samples in the 8–9 R_E bin is evident due to the spacecraft apogee location.

[12] The fluxgate magnetometer [*Potemra et al.*, 1985] on board CCE acquired data at a sampling rate of 8 vectors s^{-1}, with one component along the satellite spin axis and two components in the spin plane. The vector samples were rotated from the spacecraft coordinates into the geocentric solar ecliptic coordinate system and averaged down to a 5.9 s resolution to match the spin period of the spacecraft [*Takahashi and Strangeway*, 1990; *Takahashi et al.*, 2002] (http://sd-www.jhuapl.edu/AMPTE/MAG/).

[13] The spin-averaged field data provided in a daily format were reorganized into orbital format (the data were sliced at each perigee pass). Since the toroidal frequencies of equation (1) are found to be proportional to the magnitude of the magnetic field ($f_n \sim B/\sqrt{\rho}$) in the Wentzel-Kramers-Brillouin (WKB) approximation, the frequency variation between inbound and outbound orbits will be roughly symmetric with respect to the apogee and thus organizing the data in an orbital format makes it easier to extract the toroidal frequencies. During this process, data for $L < 4$ were discarded due to the sampling rate of the magnetometer (the second or third harmonic at $L = 4$ is at about the Nyquist frequency) and the increased orbital speed of the spacecraft.

[14] The reorganized data were then resampled with a sampling frequency, $f_{sample}(t)$ (explained later in this section) that varied with time. The resampling process is done as follows. Letting t_{start} and t_{end} be the start and end times of each orbit, we first set a time axis, t_i, such that $0 \le t_i < t_{end} - t_{start}$. At each time segment, t_i, we resample the entire data at a sampling rate given by $f_{sample}(t_i)$ and then rotate the resampled data into mean-field-aligned (MFA) coordinates where $\mathbf{e}_z$ is along the mean field defined by the running averages of the resampled data over a 1536 second window, $\mathbf{e}_x$ is radially outward in the plane containing the mean field and the spacecraft position vector, and $\mathbf{e}_y$ is eastward completing the right-hand rule. Practically, we only need to resample window length wide (plus extra padding for the running average) data segment centered at t_i. Finally, the mean field is subtracted from the rotated field to get the waveform. Note that the sampling rate remains fixed in a given window.

[15] Figure 2a shows the azimuthal component of Fast Fourier Transformed (FFT) power spectral density with $f_{sample}(t)$ fixed to 1/6 s^{-1}. A 128 point hamming window was multiplied with the waveform before the Fourier transform. Five harmonic frequencies can readily be inferred, even though the spectral power at the fourth frequency, f_{T4}, is faint. Starting at 80 mHz at the beginning of the spectrogram, the third harmonic frequency, f_{T3}, which is most prominent, decreases to about 25 mHz at apogee, shown near the center of the spectrogram.

[16] Due to the large variation of the frequency as a function of L value, it is difficult, especially for the automatic frequency identification, to extract the toroidal frequencies consistently across the L values. For example, in Figure 2a, the frequency separation at apogee is too small to resolve discrete harmonics (even though this example shows relatively clean harmonic structure which is not always the case). To have the automatic detection work reliably, we scaled the sampling rate by choosing a simple parabolic function for f_{sample}, given by $1/f_{sample}(t) = 12 + (6 - 12) \times (2t/(t_{end} - t_{start}) - 1)^2$. The maximum and minimum sampling frequencies were set to 1/6 and 1/12 s^{-1}, respectively. This scaling is equivalent to increasing the window length as the spacecraft moves to the apogee. The resulting power spectra then have an increased frequency resolution around the

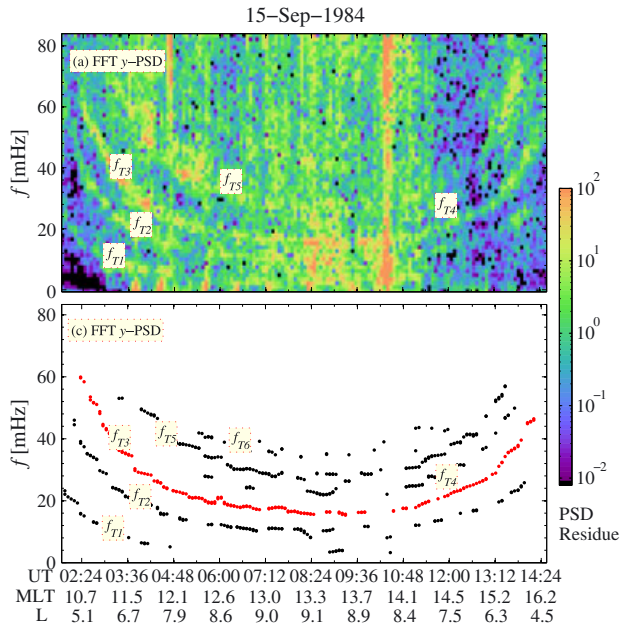

Figure 2. Toroidal Alfvén waves observed on 15 September 1984. (a) FFT power spectra and (b) the identified toroidal frequencies. The red dots shown on Figure 2b indicate the third harmonic frequencies. For a better identification of the spectral features, the residual power is shown.

apogee where the harmonic frequencies are closely spaced. We tried f_{sample} based on the WKB approximation but the result was not satisfactory. The simple parabolic function for f_{sample} was determined by examining the pattern of the frequency variations.

[17] We also used the power spectra obtained using the maximum entropy method (MEM) [*Ulrich and Bishop*, 1975; *Press et al.*, 1992]. This technique was used in *Takahashi et al.* [2010] and their related previous papers, and proved to be more practical than previous methods in that: (1) the spectra is given in an analytical form, and (2) the spectral peaks are sharply defined. MEM is identical to the autoregressive spectral analysis and the best MEM order can be determined by using a criterion called Akaike Information Criterion at each time MEM is applied [*Ulrich and Bishop*, 1975]. In this paper, however, a fixed MEM order 15 was used after several experiments.

[18] We found that the third harmonic frequencies, f_{T3}, were most common in the data set. Similar to *Takahashi and Denton* [2007] and *Takahashi et al.* [2010], we selected the f_{T3} samples to which all other identified frequencies were normalized. The selection of f_{T3} is different from *Takahashi et al.* [2002] who used the fundamental frequency (f_{T1}) identified mainly from the energetic particle flux anisotropy (proxy of transverse electric field) obtained from the Medium-Energy Particle Analyzer data.

[19] For the automatic detection, we applied the same constraints as *Takahashi et al.* [2010] to distinguish the frequencies at real peaks from those due to noise. That is, we counted the frequency, f_{peak}, at the peak of y component of the spectral power P_y as a toroidal mode spectral peak only if $P_y > P_z$ and $P_y > 3P_x$, and $\Delta f_{\text{peak}} \leq 3$ mHz, where Δf is the full width at half maximum. After the automatic algorithm filtered out the frequency at the toroidal mode spectral peak, the f_{T3}'s were then manually selected by visual inspection. Shown in Figure 2b are the automatically detected f_{peak}'s among which the manually selected f_{T3}'s are colored in red. As is clear from the figure, the automatic algorithm was able to detect all the frequency structure in this sample.

[20] We also followed the aforementioned automatic procedure with a window length of 200 points for comparison. The resulting f_{peak}'s from both results were almost identical. We used both results for manually choosing f_{T3} because (1) one result can be cross-checked by another and (2) there are often cases where superimposing two results seamlessly connect the continuous f_{T3} line as well as other f_{peak} lines by filling each other's missing gaps. In the above example, these peaks were identical because the spectral peaks were well defined.

3.2. GOES

[21] In addition to the CCE data, we also used GOES vector magnetic field samples from the GOES 10, 11, and 12 magnetometer data [*Singer et al.*, 1996]. While GOES magnetometer data have been available for decades, special efforts provided an approximate 2 year interval (during 2007 and 2008) of continuous high-resolution 0.5 s data that are used in this study. The primary purpose for using this data set is for (1) validation of our harmonic identification process by comparing our GOES statistics with those of *Takahashi and Denton* [2007] and *Takahashi et al.* [2010], and for (2) cross-checking the derived equatorial density from the CCE data set at geosynchronous orbit, again for verification purpose. Since both missions were operating during solar minimum (Figure 3), the GOES data set should be a suitable choice for this purpose.

[22] Figure 1b shows the spatial coverage of GOES 10, 11, and 12 as a function of MLT. The MLT is binned in steps of 1 h and the number of samples at each bin and each spacecraft is normalized to the maximum number of samples of all bins and all spacecraft. Except that GOES 10 sampled the magnetic field less frequently than the other two spacecraft, the magnetic field samples are evenly distributed in MLT ($\leq$ 5% variation).

[23] The data were provided with 0.512 s resolution in the Geocentric Solar Magnetospheric coordinate system. Each data set was combined and sliced at 0000 MLT to have the magnetic field samples organized in MLT, and processed similarly to the CCE data. The f_{sample} was fixed to 1/8 s^{-1} in this case because the radial distance should not change at all. The GOES data usually have very well defined spectral peaks and we used the window of length 256 points for both FFT and MEM spectra.

3.3. Solar and Geomagnetic Activity

[24] Following the results obtained by *Takahashi et al.* [2010], the underlying mass density is highly correlated with the long-term solar cycle variation and somewhat weakly correlated with the short-term geomagnetic activity. In contrast to their study though, our data set was obtained during solar minimum throughout most of the mission period as shown in Figure 3. Most of the time that CCE was operating was during solar minimum; near the end of its operation, the solar cycle was in the rising phase of solar activity. In

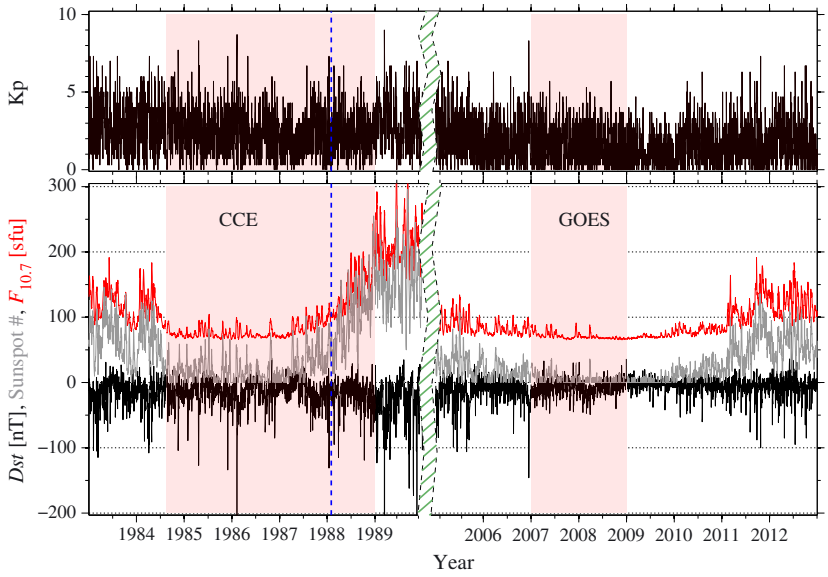

Figure 3. Solar and geomagnetic activity during the CCE and GOES mission periods used in this study. One day-averaged 1 h OMNI data (hourly resolution, multi-source data set; http://omniweb.gsfc.nasa.gov) were used to produce the plot. (top) *Kp*, (bottom) $F_{10.7}$ (red), sunspot number (gray), and *Dst* index (black). The shaded boxes indicate the periods that data were acquired. The vertical dashed line is drawn on 1 February 1988.

this paper, we excluded the CCE data after February 1988 (indicated by the vertical dashed line in the figure) for the statistical analysis to focus on the mass density variation during the solar cycle minimum. The GOES satellites were also operating during the solar minimum, as indicated by the shaded area on the right half of the figure. Comparing the geomagnetic and solar activity side by side, the period of the GOES interval was quieter than that of the CCE operation: $F_{10.7}$, *Dst*, and the sunspot numbers were more stable during the GOES interval.

4. Statistical Characteristics of f_{T3}

[25] Figure 4 shows the radial and local time distribution of the identified f_{T3} samples from the CCE data set. As in *Takahashi et al.* [2002], the distribution of the f_{T3} samples in our data set is biased toward the dawn and prenoon sectors and is bound within $L \sim 10$. Unlike their distribution of the f_{T1} samples, a substantial number of the measurements of f_{T3} in our data set are located within geosynchronous orbit (GEO), but very few are found between 1800 and 0300 MLT. In fact, the toroidal waves were rarely found around midnight in our data set (shaded area). This may be one weakness of using the magnetic field data in isolation [*Denton et al.*, 2001, 2004a].

[26] It is important to evaluate the detection rate of f_{T3} because the intensity of toroidal waves depends on the MLT and L values [*Takahashi et al.*, 2002, 2010]. MLT was divided into 24 equally spaced, nonoverlapping bins, and the L shells were divided into three equally spaced, nonoverlapping bins: $4 < L < 6$, $6 < L < 8$, and $8 < L < 10$. At each bin, we calculated the ratio of the number of the f_{T3} samples to the available magnetic field data segments.

[27] Figure 5a shows the f_{T3} detection rate for the data set from the three GOES satellites. The three curves almost coincide each other, indicating the consistent frequency detection among three satellites. The subtle difference can be attributed to the discrete GOES satellite location in magnetic latitude (MLAT) [*Takahashi and Anderson*, 1992; *Takahashi et al.*, 2010]. Figure 5b shows the MLAT histogram of three GOES satellites. MLAT was binned in steps of 2° with no overlap. The MLAT distribution of GOES 11 makes a sharp peak at 5°, while that of GOES 10 and 12 spans from 9° to 11° and from 7° and 13°, respectively. Considering that

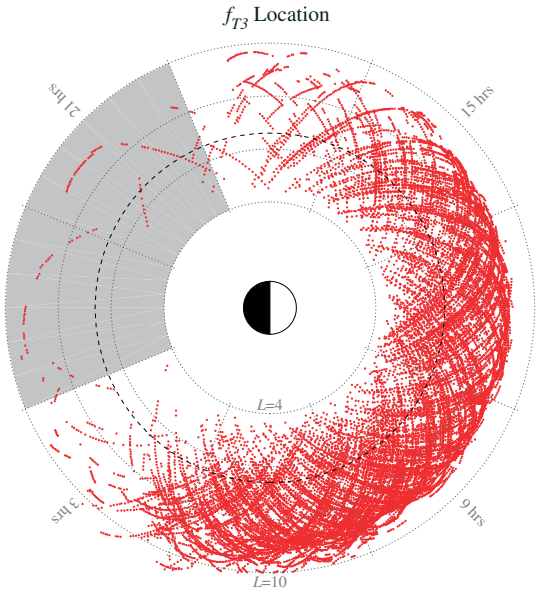

Figure 4. The distribution of the CCE f_{T3} samples within the range L = 4–10. The dotted concentric circles are drawn at every 2 R_E and the dashed circle is at 6.6 R_E. The gray area at midnight indicates a region having a small number of f_{T3} samples.

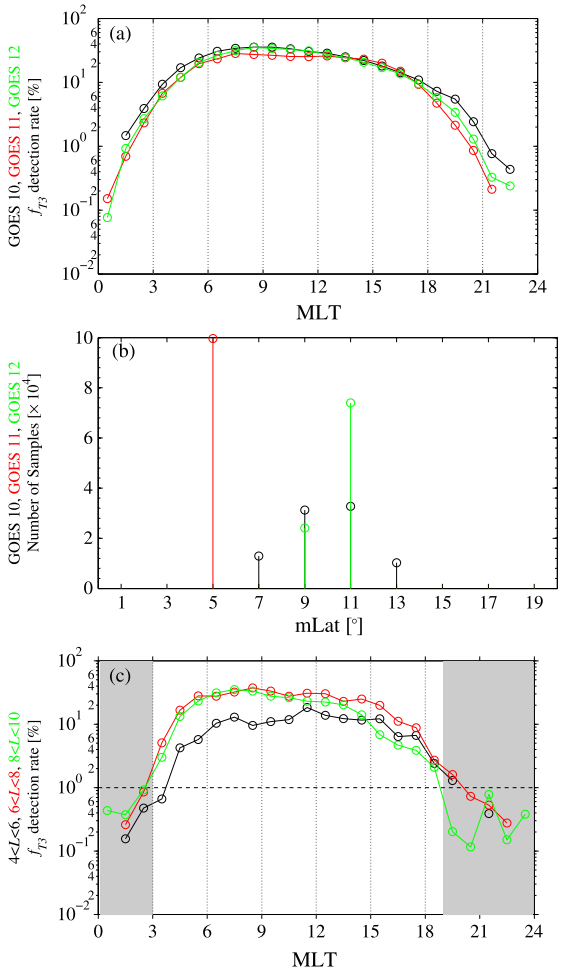

Figure 5. The f_{T3} detection rate as a function of MLT calculated from the (a) GOES and (c) CCE magnetometer data and f_{T3} samples, and (b) the GOES magnetic latitude histogram. (Figures 5a and 5b) The rates and the magnetic latitude histogram for GOES 10, 11, and 12 satellites are colored in black, red, and green, respectively. (Figure 5c) The rates for $4 < L < 6$, $6 < L < 8$, and $8 < L < 10$ bins are colored in black, red, and green, respectively. Where the detection rate is roughly below 10% is shaded.

the toroidal mode has a B_y node at the magnetic equator and its amplitude increases monotonically toward an antinode located at MLAT > 10° [*Cummings et al.*, 1969], the order of the detection rates, GOES 10 ≥ GOES 12 > GOES 11, may be explained by their latitudinal location. Compared to *Takahashi et al.* [2010, Figure 5b], our result reproduces all the essential features of their analysis. Namely, the detection rate is high in the prenoon sector, exceeds 10% between 0300 and 1800 MLT and tapers off toward midnight. These authors suspected that the bias of the detection rate toward the morningside is probably related to the upstream ULF waves in the foreshock region and the orientation of the interplanetary magnetic field (IMF) which statistically follows Parker's spiral. Another likely cause of the bias is a region of high-density plasma at the post-noon sector, which lowers not only the toroidal frequencies but also the interval of the two adjacent frequencies. In fact, there were quite a few occurrences of the tight harmonic structure in our data set. The MEM spectra with the current settings did not separate them clearly, nor did visual inspection. We excluded these spectra to avoid false identification of f_{T3}. As a result, the averaged mass density presented in this paper, particularly at post-noon sector, may be underestimated.

[28] Figure 5c shows the f_{T3} detection rate for the CCE data set. The detection rate for $L > 6$ is very similar to that of the GOES data set and that for $L < 6$ is slightly lower in magnitude, but has essentially the same variation with MLT. The fast transition of the spacecraft in the inner magnetosphere can cause broadening of spectral peaks of the processed spectra and these peaks do not satisfy the Δf constraint. Compared to *Takahashi et al.* [2002], the number of f_{T3} samples at the nighttime sector is much lower than the number of their f_{T1} samples. As mentioned earlier, the processing issue and use of the magnetometer data in isolation rather than the existence of the toroidal waves could result in the lower detection rate. The region where the detection rate for CCE is less than roughly 10% is indicated by a shaded box, and the result in this region may not be statistically significant in this study.

[29] As an example, Figure 6 shows samples of the identified frequencies and the normalized frequencies to f_{T3} as a function of MLT. For GOES (Figure 6a), a quarter of GOES 10 samples were used, and for CCE (Figure 6b), samples from $6 < L < 7$ for the first year were used to produce the figure. In Figure 6a (top), the data points are mixed and scattered although the lower three harmonic frequencies are separable. When normalized to f_{T3} in Figure 6a (bottom), up to six harmonic frequencies are cleanly organized and the distribution is sharp around each toroidal frequency line. This result can be compared to *Takahashi and Denton* [2007, Figure 5]. The CCE samples in Figure 6b have a more disordered distribution for both unnormalized and normalized frequencies. In particular, there are quite a few data points between the regularly spaced frequency lines in the normalized frequencies. There may be two facts that come into play: noise involved in the spectral peaks and overextended L bin size. Concerning the size of the L bins, we reduced the L bin size by half and compared the result (not shown) to Figure 6b and there was a slight improvement. Given that, the false identification of noise as the toroidal frequencies and/or the uncertainty in determining the location of the spectral peaks may contribute to the dispersion to a larger degree than those of the GOES samples. Although improving the identification and determination of frequencies can be difficult, the false identification may be significantly reduced by visual inspection. In the current data processing, only the f_{T3} samples were thoroughly checked.

[30] Despite all the technical difficulties, the toroidal frequencies of the CCE data set are clearly identifiable so that the majority of the f_{T3} samples could correctly be identified as the third harmonic toroidal frequency. As *Denton et al.* [2001, 2004a] point out, using accurate toroidal frequencies is the most crucial factor for the reliable mass density derivation. The statistical results in this section may indicate that our method for detecting toroidal waves solely from magnetometer data can be applied to the data set observed over a wide range of L shells.

[31] The present paper only uses the f_{T3} samples to investigate the equatorial mass density distribution. The f_{peaks}

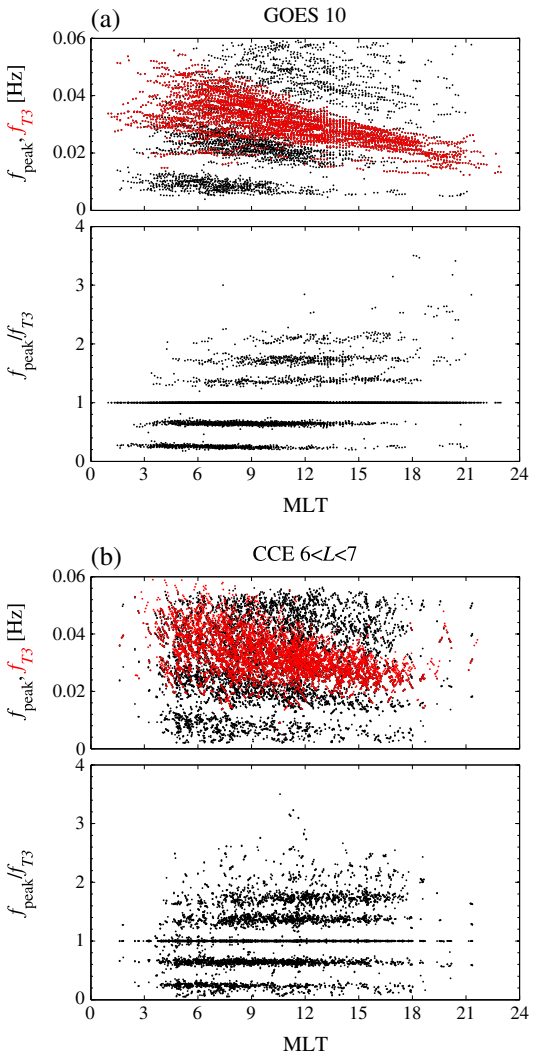

Figure 6. The automatically detected toroidal frequencies and the manually chosen f_{T3}'s as a function of MLT. (a) A quarter of the GOES 10 samples and (b) the first year of the CCE samples within $6 < L < 7$ were used to produce the plots. The (top) unnormalized and (bottom) normalized toroidal frequencies. The f_{T3} samples are indicated by red dots.

samples can, however, give us the field line variation as well [e.g., *Denton et al.*, 2006, 2007], which is currently under investigation.

5. Equatorial Mass Density, ρ_{eq}, During Solar Minimum

[32] Using the detected f_{T3} samples, we calculated the equatorial mass density using the power law model with the power law index α set to 1 [*Takahashi et al.*, 2010]. We used both dipole and T89 magnetic field models for the purpose of cross-checking although only the results for the T89 model are shown. Results for ρ_{eq} calculated using both models lie within both sets of error bars for $L \leq 7$. The difference due to the day-night asymmetry of field lines, however, becomes significant (beyond the error bar near the midnight and noon local times) for $L > 7$. Since α is fixed, ρ_{eq} in equation (2) is the only free parameter to be determined. Since there is a strong correlation between the solar radiation and ion production [e.g., *Lennartsson*, 1989, 2010], we should emphasize that our derived equatorial mass density distribution is for solar minimum conditions.

[33] To investigate the statistical characteristics of the equatorial mass density, ρ_{eq}, and f_{T3}, the median values and the interquartile ranges (IQR, the range between the first quartile and the third quartile) were calculated at each MLT and L bin. The choice of the median value and IQR is based on the study of *Takahashi et al.* [2010] and employed here for direct comparison. Throughout the analysis, MLT was binned in steps of 2 h from 1 to 24 h with 1 h overlap, and the L shells were binned in steps of $\Delta L = 1$ with L varying from 4 to 9 with no overlap. Additionally, a GEO bin at each MLT bin was defined such that the center of the GEO bin is chosen to be the median value of L of the three GOES satellites at the MLT bin. As shown in Figure 7, the L values of GOES range between 6.8 and 7.1.

5.1. Local Time Variation

[34] Figure 8a shows the variation of f_{T3} (top), ρ_{eq} (middle), and the number of samples (bottom) as a function of MLT at GEO. The median values and IQR are indicated by the open circles and the error bars. The number of the samples for CCE was more than 10 for most MLT sectors. The CCE f_{T3} median value, starting from about 40 mHz at 0300 MLT, decreases monotonically down to < 25 mHz toward 1700 MLT where it has a local minimum. A similar study based on more nightside samples by *Takahashi et al.* [2002] also showed the local minimum in frequency approximately at the same MLT. Additionally, the result therein also showed the increasing toroidal frequency toward midnight. In comparison, the GOES f_{T3} median value has the similar behavior to that of CCE except for the slightly larger magnitude and MLT of the local minimum. What caused the discrepancy in the local minimum MLT is unclear at the time of writing, but we suspect that the small number of samples of the CCE data set at the 1800–0300 MLT might have caused the discrepancy. Due to questions about the

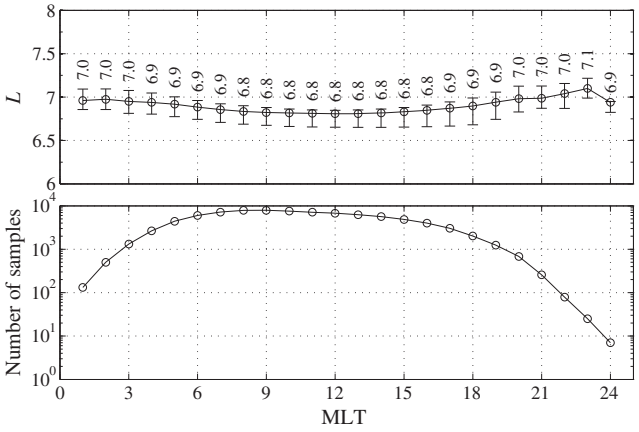

Figure 7. (top) Median values and interquartile ranges (IQR) of L of the three GOES satellites as a function of MLT and (bottom) the number of samples used to calculate the median and IQR. The numbers in Figure 7 (top) are median values at each MLT bin.

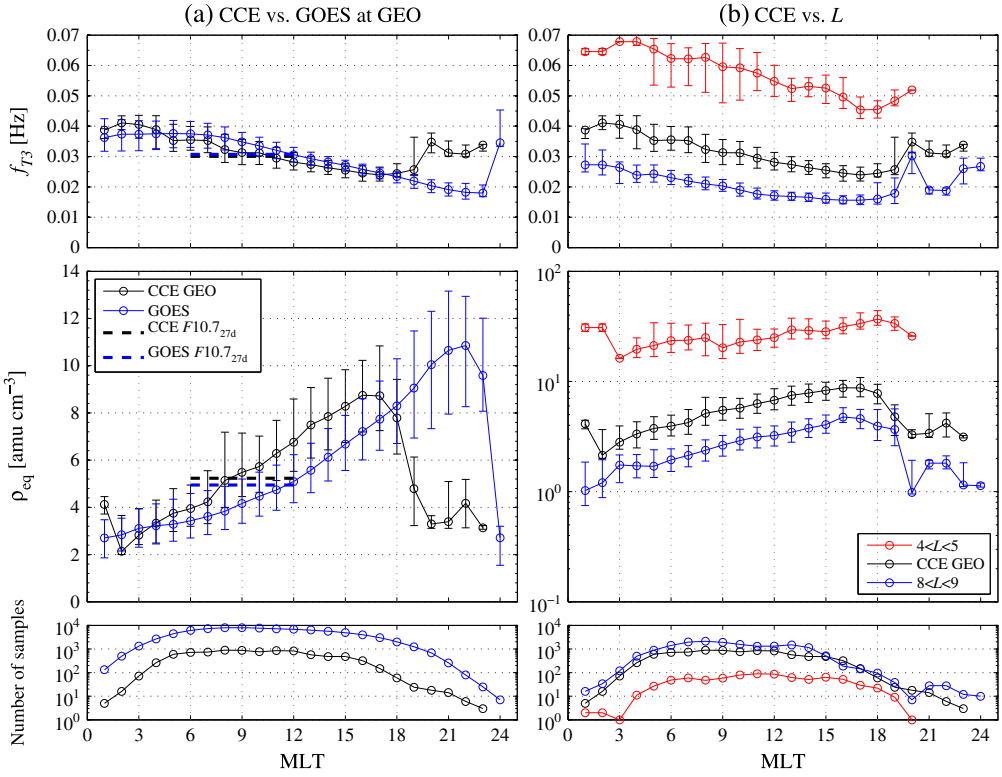

Figure 8. (top) Median values of the f_{T3} samples and (middle) the equatorial mass density, ρ_{eq}, derived from the f_{T3} samples, and (bottom) the number of the f_{T3} samples as a function of MLT. The error bars represent the interquartile range (IQR). (a) Comparison of the results between GOES and CCE for which L values vary with the L values listed at Figure 7 (top). (b) Comparison of the CCE results between three different L bins: $4 < L < 5$, GEO bin from Figure 8a, and $8 < L < 9$. The equatorial densities were calculated using the T89 field model. The dashed curves indicate 27 day-averaged equatorial mass density, $\rho_{eq,27d}$, calculated from the $F_{10.7}$ dependent empirical model (refer to section 6.2) [*Takahashi et al.*, 2010].

statistical significance, interpretation of the statistical result in the following sections only focuses on the daytime sector, i.e., 0300–1800 MLT.

[35] The derived ρ_{eq} for both data sets varies inversely with f_{T3}^2. That is, the median value monotonically increases starting below 3 amu/cm^3 at 0300 MLT toward the dusk sector up to 10 amu/cm^3. Since the field line geometries are more or less symmetric in MLT at GEO, one can intuitively expect this inverse behavior. When the dipole field is used, the daytime ρ_{eq} slightly increases owing to the shorter field line than that of the T89 field model. The slight increase of the IQR in ρ_{eq} toward the afternoon can be attributed to the choice of the linear scale comparing with Figure 8b. Since there are only a few CCE orbits in the night sector (Figure 4), the short IQR bars of ρ_{eq} for 1900–0300 MLT is likely due to all data coming from one or two orbits during which the geomagnetic condition remained constant. The noticeable difference between the median ρ_{eq} values of CCE and GOES is found in the magnitude of ρ_{eq} in the daytime sector. The maximum difference is over 2 amu/cm^3 at 1300 MLT. Brief discussion about this difference is given in section 6.2.

[36] The MLT variation can be compared to *Takahashi et al.* [2010, Figure 6]. Note that their result includes the f_{T3} samples obtained during one full solar cycle. As a result, the median value and the IQR of their ρ_{eq} are larger than ours.

[37] Figure 8b shows the MLT variation of f_{T3} and ρ_{eq} for inner and outer L bins. The figure format is the same except for the logarithmic scale in the middle. The number of samples were greater than 10 between 0400 and 1900 MLT for all L bins. One thing to immediately note is the same MLT behavior of the median value and IQR at all L bins in the daytime sector except for the difference in magnitude. The L dependence will be discussed later in this section.

[38] The L and MLT dependence of f_{T3} shown in the CCE data set has good agreement with *Takahashi et al.* [2002] whose results are based on the f_{T1} samples. Namely, the f_{T1} statistics in *Takahashi et al.* [2002] also shows a monotonic variation in local time and radial distance (Figure 6 therein).

5.2. Dependence on Geomagnetic Activity

[39] Since the geomagnetic activity can play a role in controlling ρ_{eq}, we explored the dependence of ρ_{eq} on the *Dst* and *Kp* indices, similar to the study of *Takahashi et al.* [2010]. We note that the result in this section may be affected by a bias toward the geomagnetic quiet and moderate condition as explained in section 4.

5.2.1. *Kp* Variation

[40] Figure 9a shows the dependence of f_{T3} and ρ_{eq} from GOES on Kp_{3d} which is the representative *Kp* value at the current time, t, obtained by averaging over earlier times, t', using the weighting factor $\exp(-(t-t')/t_0)$, where t_0 is 3 days.

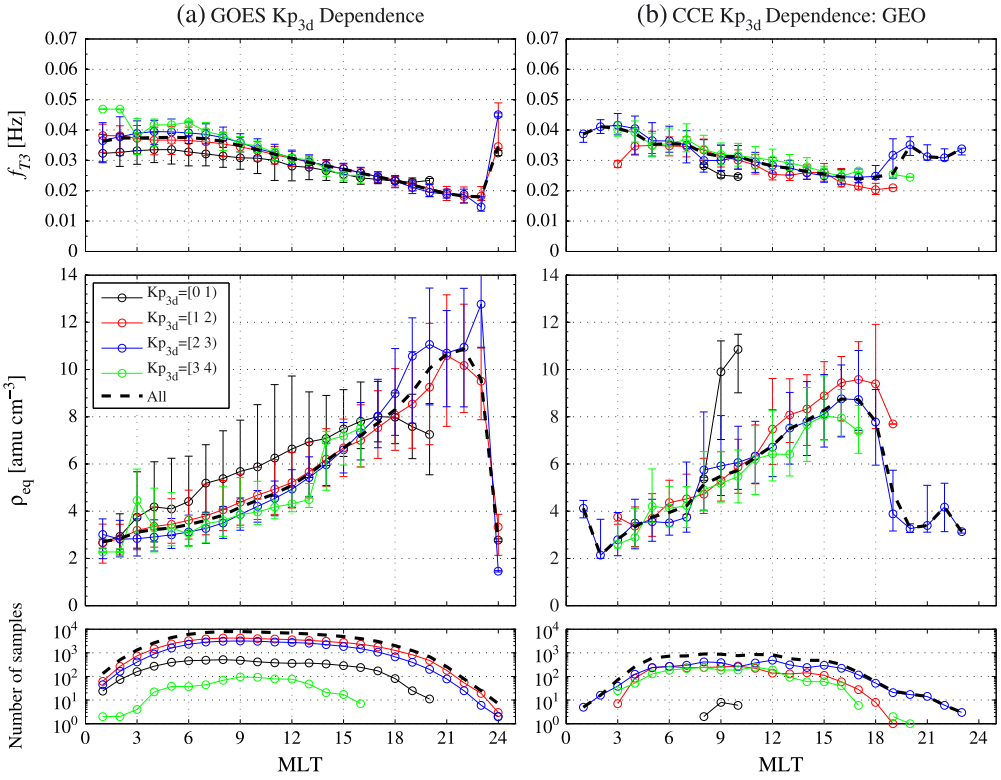

Figure 9. *Kp* dependent statistics of (top) f_{T3}, (middle) ρ_{eq}, and (bottom) the number of the f_{T3} samples as a function of MLT at geosynchronous orbit. The open circles and the error bars represent the median values and the IQR. (a) The GOES results and (b) the CCE results at $6.1 < L < 7.1$. The samples are grouped into four Kp_{3d} ranges: [0, 1), [1, 2), [2, 3), and [3, 4) that are indicated by colors. The bold dashed curves are the median values of ρ_{eq} obtained in Figure 8.

It is known that organizing ρ_{eq} by the Kp_{3d} shows better correlation than the instantaneous *Kp* value [e.g., *Denton et al.*, 2004b; *Takahashi et al.*, 2010]. We experimented with different t_0 = 0 and 1.5 days, but Kp_{3d} seems to show the trend more clearly than $Kp_{1.5d}$ and Kp_{0d}. In addition to the spatial binning, the Kp_{3d} was binned in steps of 1 from 0 to 4 with no overlap, which are represented by four colored curves. Additionally, the median values of f_{T3} and ρ_{eq} and the number of samples at GEO in Figure 8 are superimposed with the thick dashed curves.

[41] The median values of both f_{T3} and ρ_{eq} vary little for $Kp_{3d} > 1$ at all MLT. Compared to the dashed curve, the deviations are well contained within the IQR. The median values increase by 2 amu/cm^3 at maximum with the significantly larger IQR when $Kp_{3d} < 1$ in the daytime sector. This may be attributed to the refilling of the plasmasphere during extremely quiet times as discussed by *Takahashi et al.* [2010]. The usual plasma trough density observed by GOES and CCE is under 10 amu/cm^3 at the prenoon sector, which is well below than 20 amu/cm^3 set as the plasma trough density by these authors. It should be noted that our results are consistent with *Takahashi et al.* [2010, Figure 9].

[42] Figure 9b shows the same Kp_{3d} dependence for CCE at GEO. The deviations of f_{T3} and ρ_{eq} for $Kp_{3d} > 1$ are well contained within the IQR as for the GOES case. In the CCE case, however, the number of samples for $Kp_{3d} < 1$ was extremely small, so the results may not be statistically meaningful.

[43] Figures 10a and 10b show the Kp_{3d} dependence in the inner (L = 4.5 bin) and outer (L = 8.5 bin) L shells, respectively. The figure format is the same as the previous figure, and additionally, the dash-dotted curves in Figures 10a and 10b represent the median values of the inner and outer L shells from Figure 8, respectively. As can be anticipated, both results are only weakly correlated with the *Kp* index although the result in Figure 10a may not be statistically significant due to the small number of samples. The outlier within the shaded box reach up to 150 amu/cm^3 and will be discussed in section 6.1.

5.2.2. *Dst* Variation

[44] Figures 11a and 11b show the *Dst* dependence for GOES and CCE at GEO in the same manner as Figure 9. In addition to the spatial binning, the data were divided into three groups according to *Dst*: $-500 < Dst < -50$, $-50 < Dst < -10$, and $-10 < Dst < 100$ nT at each of which the median values and IQR were calculated as before. For GOES, the median values of f_{T3} and ρ_{eq} are almost identical for quiet or moderately disturbed times. It is when $Dst < -50$ nT that the deviation becomes substantial. *Takahashi et al.* [2010] speculated that this deviation most likely results from storm injection of heavy ions. Unlike the GOES case, the CCE data (Figure 11b) shows that ρ_{eq} for $Dst > -10$ nT at MLT of the local maximum is slightly larger than that for $Dst < -10$ nT.

[45] Figures 12a and 12b show the *Dst* dependence in the same manner as Figure 10. In the inner magnetosphere,

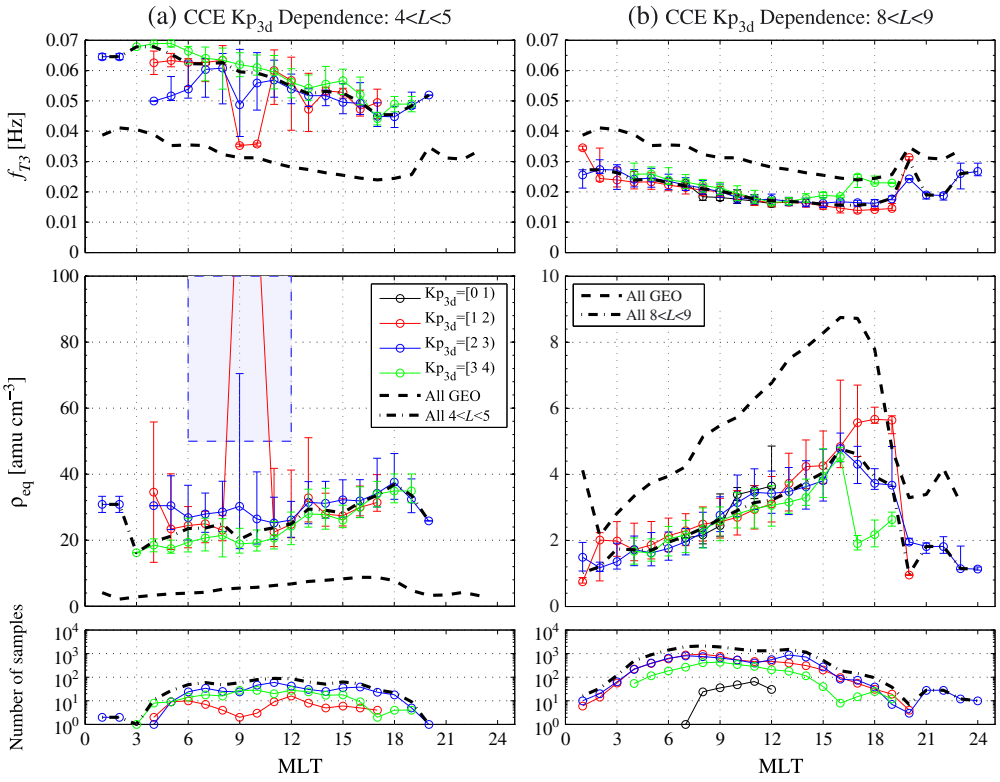

Figure 10. *Kp* dependent statistics at inner and outer L shell regions: (a) $4 < L < 5$ and (b) $8 < L < 9$. The figure format is the same as Figure 9. The dashed curves are the median values of ρ_{eq} at the GEO bin and the dash-dotted curves are the median values of ρ_{eq} at either $4 < L < 5$ (Figure 10a) or $8 < L < 9$ (Figure 10b). The significant outlier samples are indicated by the shaded box.

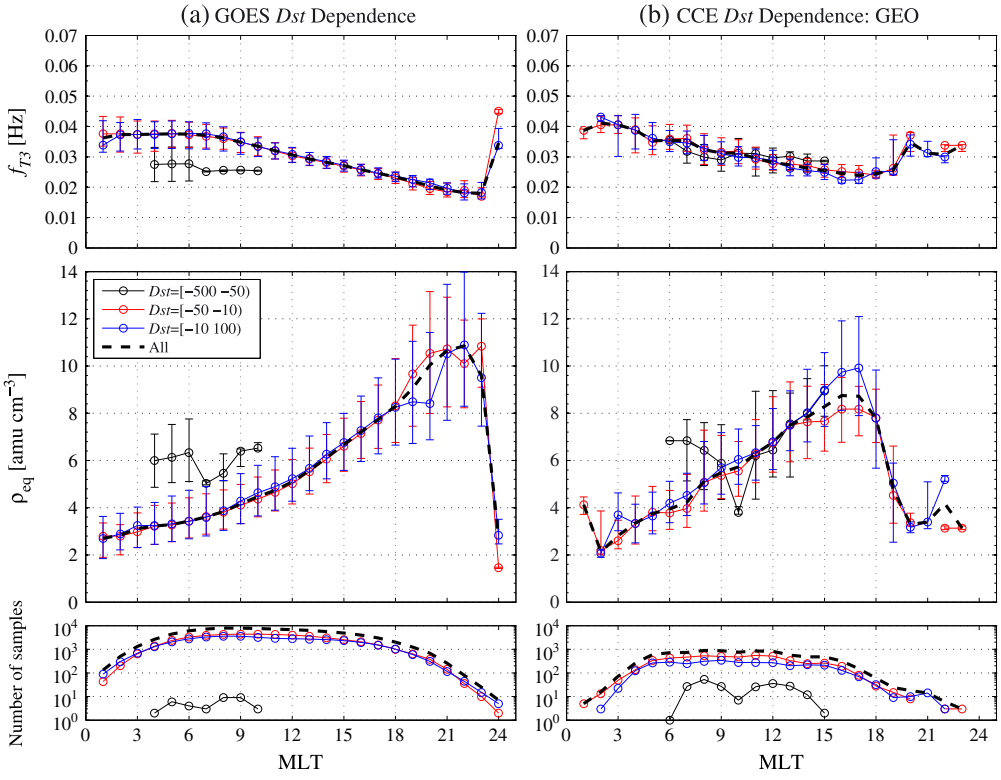

Figure 11. Same as Figure 9 but for *Dst* dependence. The samples are grouped into three *Dst* ranges: [–500, –50), [–50, –10), and [–10, 100) nT.

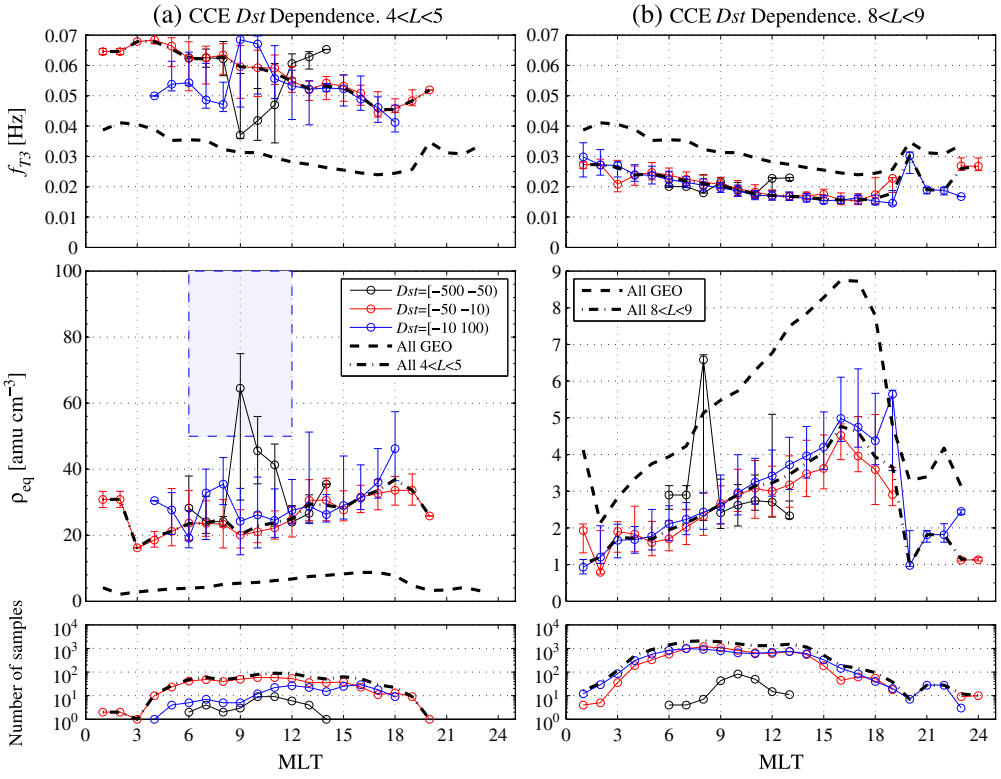

Figure 12. Same as Figure 10 but for *Dst* dependence. The samples are grouped into three *Dst* ranges: [–500, –50), [–50, –10), and [–10, 100) nT. The shaded box represents significant outliers that are discussed in section 6.1.

the median values are weakly correlated to the *Dst* except for strongly disturbed times. The largest ρ_{eq} in the data set was about 180 amu/cm^3 and contributed to the outlier in the shaded box (Figure 12a). In the outer magnetosphere, the deviations over a large range of MLT for *Dst* > –50 nT (blue and red curves) are somewhat larger than those at GEO even though they are within the IQR.

5.3. *L* Variation

[46] Since the CCE data set provide a unique opportunity to investigate the radial variation of ρ_{eq}, it has been further investigated at four selected MLT bins in the daytime sector.

[47] Figure13 shows the variation of f_{T3} and ρ_{eq} in *L* value in the same format as the previous figures. The figure is divided into four groups corresponding to four MLT bins, and to reduce confusion, the panels in each group have the same background color. At all MLT bins, it is clear that f_{T3} and ρ_{eq} monotonically decrease in the linear space and logarithmic space, respectively. Statistical studies using the ground-based ULF observation also show that the mass density falls logarithmically with *L* value in the inner magnetosphere [*Berube et al.*, 2005; *Waters et al.*, 2006]. The ρ_{eq} variation in *L* value was approximated with the second-order polynomial at each MLT. The fitting coefficients in Table 1 suggest a strong linear correlation, as was expected. The dashed curves in the figure show the approximated ρ_{eq}.

[48] The radial dependence shown in Figure 13 can be compared to Figure 12 in *Takahashi and Anderson* [1992]. Similar to our analysis, these authors derived the mass density as a function of *L* value using equation (2) and the toroidal frequencies from the CCE magnetometer data. These authors, however, used $\alpha = 4$ as the power law index and used a dipole background magnetic field, and therefore, only qualitative comparison is possible. The figure shows a steep gradient in ρ_{eq} at about $L = 4.2$ beyond which it decreases logarithmically. The magnitude of our ρ_{eq} for $L = 5$–6 at both 0900 and 1200 MLT sectors is slightly larger than that of *Takahashi et al.* [2010] in 0900–1200 MLT sector, which may be attributed to the different assumptions. ρ_{eq} of GOES is also superimposed for a reference at $L = 6.6$, which is lower at the daytime sector as was anticipated from Figure 8; but the range of the error bars overlaps.

6. Discussion

6.1. Short-Lived ρ_{eq} Enhancement and Solar Cycle Variation

[49] Since CCE detected the toroidal waves during the rising phase of the solar cycle as well, we briefly discuss the solar cycle variation of ρ_{eq}. Figure 14a shows all ρ_{eq} samples, including those during the rising phase of solar cycle at the end of the mission period, of CCE for $L < 6$ (bottom) and the related *Kp*, *Dst*, and $F_{10.7}$ (top and middle). The units of $F_{10.7}$ are 10^{-22} W/m^2 Hz, referred to as the solar flux units (sfu). During the solar cycle minimum, the samples had values of ρ_{eq} less than 50 amu/cm^3 for the $L = 4.5$ bin and less than 30 amu/cm^3 for the $L = 5.5$ bin. The median value of all ρ_{eq} samples shown in the figure is 20 amu/cm^3 indicated by the horizontal dashed line. During the rising phase of the solar cycle after January 1988, it is clear that ρ_{eq} on average increased compared to the median value. One can also notice

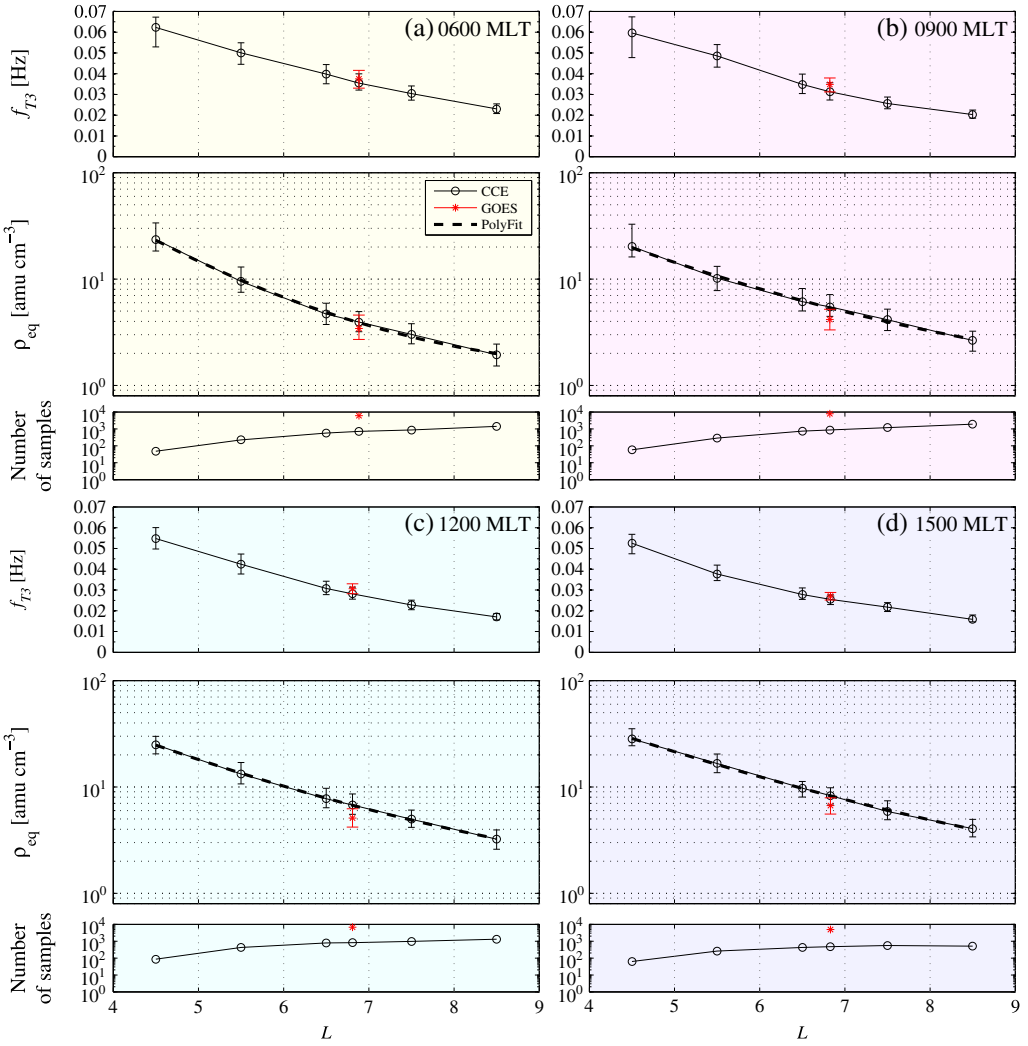

Figure 13. *L* dependent statistics at four selected MLT ranges: (a) 0500–0700, (b) 0800–1000, (c) 1100–1300, and (d) 1400–1600 MLT that are indicated by four light colors. The format is the same as Figure 8. The GOES results are superimposed at 6.6 R_E. The dashed curves on the ρ_{eq} panels are the quadratic polynomial fit whose coefficients are tabulated in Table 1.

the annual variation of ρ_{eq}. This can be attributed to the precession of the CCE orbit. Overall, this figure clearly shows the strong correlation of ρ_{eq} with the long-term solar cycle variation as shown by *Vellante et al.* [2007] and *Takahashi et al.* [2010].

[50] Sporadic density enhancements with ρ_{eq} greater than 50 amu/cm^3 in the figure are believed to be related to the plasmaspheric expansion and/or geomagnetic storms. *Takahashi et al.* [2010] isolated these two effects by carefully inspecting the baseline of ρ_{eq} in relation to *Kp* and *Dst* and concluded that these enhancements are short-lived and usually occur during very quiet or severely disturbed times. They claimed that the enhancements due to the former are related to the refilling of the plasmasphere and the enhancements due to the latter are related to heavy ion (O^+) injection. Figure 14b shows the examples of these enhancements that occurred for about 5 months indicated by the shaded box (Figure 14a) including several strong storms. Particularly, one enhancement in the beginning of January 1886 (the dashed line) accompanied a significant *Dst* drop. ρ_{eq} increased up to about 180 amu/cm^3 prior to the negative *Dst* $\sim$ –100 nT and the Kp_{3d} increased to about 2. Note that the absence of mass enhancements for other storms does not necessary imply that no enhancement occurred, but could be due to the magnetometer of CCE not detecting the toroidal mode waves or being located at the wrong position during those storms. Since the plasmapause certainly moves inward during the main phase of storm, these enhancements are likely associated with the heavy ions injected into the inner magnetosphere during the main phase of geomagnetic storms, as also confirmed by the CRRES observation of the toroidal waves [*Takahashi et al.*, 2006].

Table 1. Fitting Coefficients of Logarithmic *L* Dependence[a]

MLT	p_1	p_2	p_3
0600	0.0328	–0.6995	3.8379
0900	0.0193	–0.4746	3.0459
1200	0.0111	–0.3749	2.8651
1500	0.0103	–0.3543	2.8446

[a]The polynomial model is given by $\log_{10} \rho_{eq,fit}(L) = p_1L^2+p_2L+p_3$ where the units of $\rho_{eq,fit}$ are amu/cm^3.

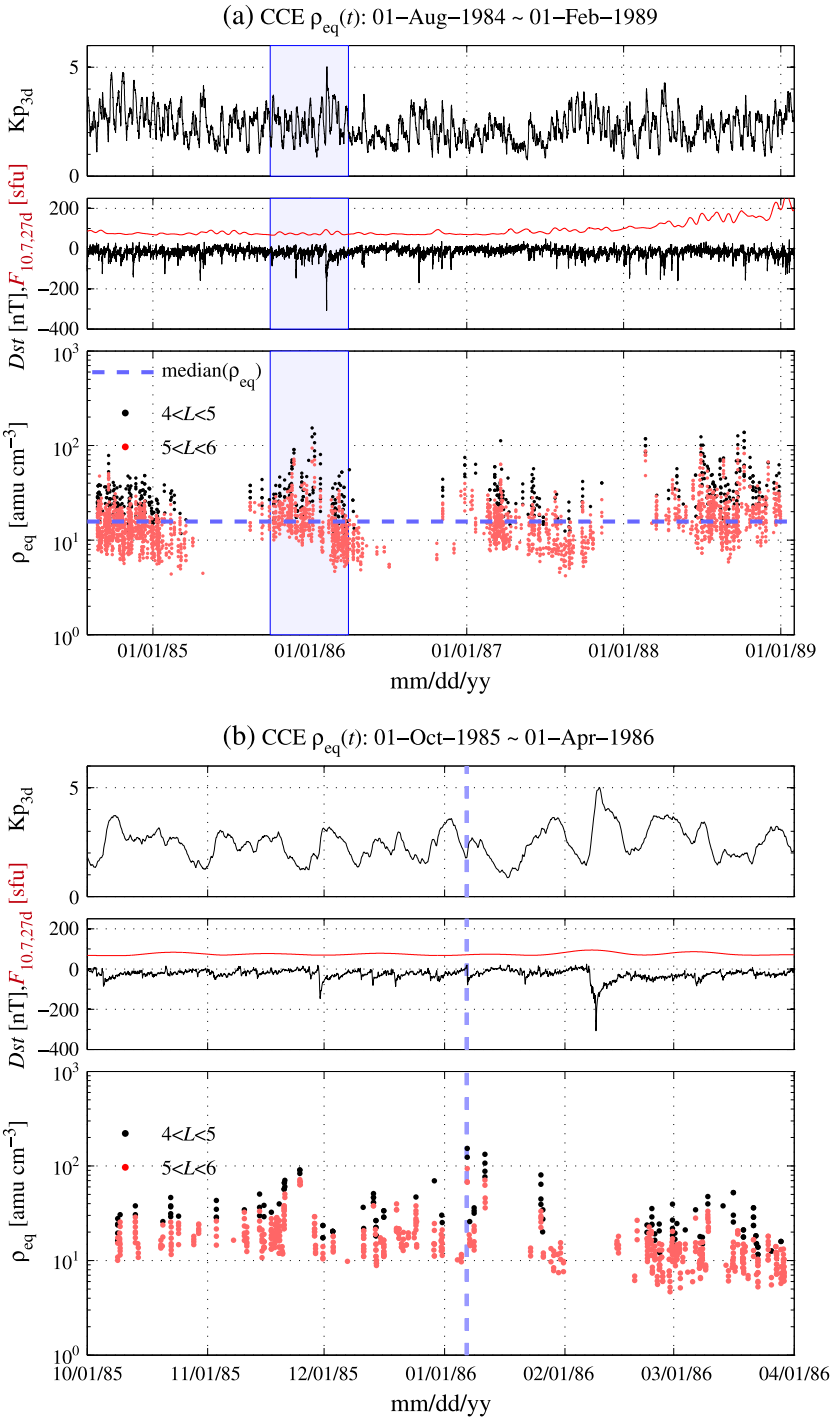

Figure 14. The ρ_{eq} samples that caused the significant outliers in Figures 10 and 12. (a) Shown are ρ_{eq} samples from CCE for $4 < L < 6$ and the corresponding Kp_{3d}, Dst, and $F_{10.7,27d}$ (27 day-averaged $F_{10.7}$) [*Takahashi et al.*, 2010] parameters for whole years. The shaded boxes indicate the period that has substantial ρ_{eq} enhancements. (b) The same as Figure 14a but the time axes are magnified to fit to the shaded boxes. The dashed line in Figure 14a (bottom) indicates 6 January 1986.

6.2. Comparison With $F_{10.7}$-Based Empirical Model

[51] The strong correlation of ρ_{eq} with the solar activity has been investigated in previous studies [*Vellante et al.*, 1996, 2007; *Takahashi et al.*, 2010]. It is known that the solar irradiation (UV/EUV) is a major controlling factor of ionospheric outflows and thus ion production [*Strangeway et al.*, 2005]. Based on the result of the strong correlation with long-term variations of $F_{10.7}$, *Takahashi et al.* [2010] established a simple empirical model of f_{T3} and ρ_{eq} that can be written as

$$f_{T3,27d} = 37.5 - 0.0972F_{10.7,27d}, \quad (3)$$

$$\log_{10}(\rho_{eq,27d}) = 0.421 + 0.00390F_{10.7,27d}, \quad (4)$$

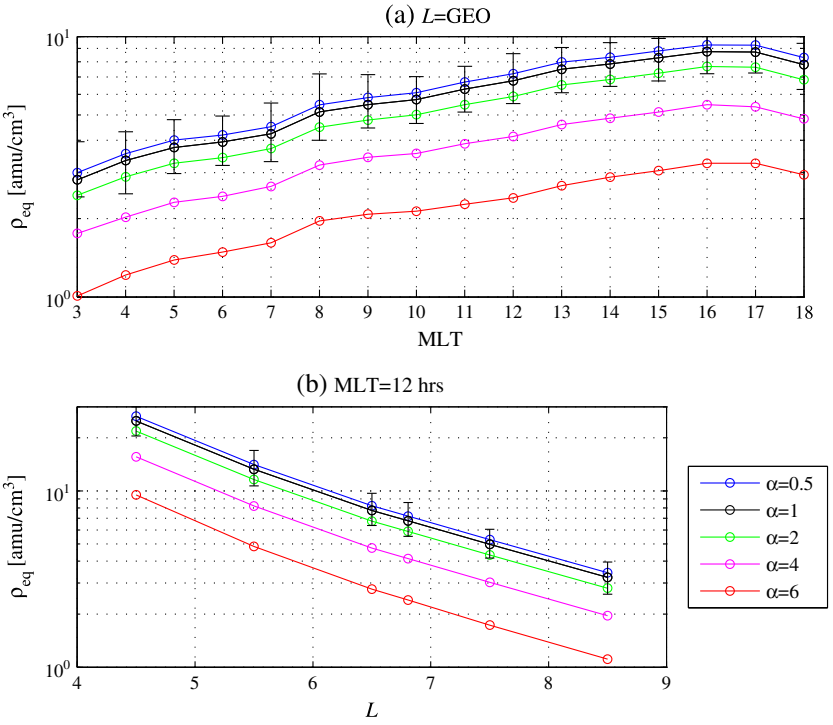

Figure 15. Dependence of ρ_{eq} on different values of the power law index, α. (a) ρ_{eq} as a function of MLT at GEO and (b) ρ_{eq} as a function of L shell at noon MLT. The results of five different α values (0.5, 1, 2, 4, and 6) are represented by blue, black, green, red, and magenta colors.

where units of $f_{T3,27d}$, $F_{10.7,27d}$, and $\rho_{eq,27d}$ are given by mHz, sfu, and amu/cm^3, respectively, and the variables are all 27 day averaged as indicated by the subscript. The calculated $f_{T3,27d}$ and $\rho_{eq,27d}$ represent the nominal values at the dawn-noon sector.

[52] The thick dashed curves in Figure 8a shows the median values of $f_{T3,27d}$ and $\rho_{eq,27d}$ that were calculated from $F_{10.7,27d}$ at each sample in the dawn-noon sector. The model well estimates the derived mass density at 1000 MLT for CCE but overestimates the density at all dawn-noon local times for GOES. The CCE data was collected during the time period of the data set of *Takahashi et al.* [2010] (1980–1992) which was used to find equation (3) and (4). On the other hand, our GOES data set was taken during the recent solar cycle minimum. When comparing these two solar cycle minima in Figure 3, average $F_{10.7}$ for GOES is only slightly lower than that for CCE although $F_{10.7}$ for CCE has more spikes. The sunspot number and *Dst* indicate that the solar activity during the recent solar minimum was much quieter than the one for CCE, which may have led to lower ρ_{eq} for GOES.

6.3. Dependence of ρ_{eq} on the Power Law Index α

[53] In order to investigate how variations in α affect the derived ρ_{eq}, we calculate ρ_{eq} for four additional α values, 0.5, 2, 4, and 6. Figure 15a shows the ρ_{eq} dependence on different α values as a function of MLT at GEO. The black curve shows the result for $\alpha = 1$. Clearly, as α increases from 0.5 to 6, ρ_{eq} decreases: the ratio $\rho_{eq}(\alpha = 1)/\rho_{eq}(\alpha = 6)$ is about 3. The deviations for $\alpha = 0.5$ and 2 are within the estimated error range of ρ_{eq} with $\alpha = 1$. These variations are consistent across L shells and MLT bins as shown in the figure.

[54] *Denton et al.* [2006] investigated the effective α values and found that $\alpha = 2$ is appropriate for $L = 4 – 5$ ($\alpha = 1$ for $L = 5 – 6$) for the mass density field line distributions. For $L > 6$, none of α values are appropriate because the field line distributions become nonmonotonic with a local peak in mass density at the magnetic equator [*Takahashi et al.*, 2004]. *Takahashi et al.* [2006] and *Denton et al.* [2006] suggested that if one chooses to use the power law model for $L > 6$, the $\alpha = 1$ solution better characterizes the distribution along the entire field line. We note that their studies are based on CRRES data predominantly at solar maximum in the afternoon local time sector.

[55] The effective α values also depend on MLT. *Takahashi and Denton* [2007] examined the local time dependence of the mass density distributions using GOES data and found that the equatorial peak occurs in the dusk sector but not in the dawn sector. This may suggest a larger α value in the dawn sector due to the mass density minimum at the magnetic equator.

[56] Based on the previous studies, larger α values appear to be appropriate in the inner magnetosphere and/or in the dawn sector, where the mass density distributions are monotonic with a local minimum at the magnetic equator, than those in the outer magnetosphere and/or in the dusk sector, where the distributions are nonmonotonic with a local peak at the magnetic equator. Assuming that the effective alpha value tends to decrease toward the dusk sector and/or the larger L value, the resulting local time (radial) variation would become more rapid (slower) than the result with $\alpha = 1$.

7. Summary

[57] We have determined the global variation of the equatorial mass density derived from the toroidal Alfvén frequencies acquired by GOES satellites during solar minimum and CCE during solar minimum and the rising phase of the solar cycle. The frequency observations from CCE enabled us to investigate the L shell dependence of the mass density in the outer magnetosphere between $L = 4$ and 9, providing a more thorough understanding of the global structure of the equatorial mass density. The third harmonic frequency, f_{T3}, was used to derive the equatorial mass density, ρ_{eq}, assuming the power law variation along the field line with $\alpha = 1$ for the inversion technique. Our analysis procedure and frequency identification algorithm were thoroughly cross-checked with the result of *Takahashi et al.* [2010], and between the CCE and GOES samples at GEO. To increase the statistical significance of our results, this study only focused on the 0300–1800 MLT.

[58] We summarize our main findings:

[59] 1. The MLT variations of f_{T3} and ρ_{eq} at GEO observed by two different missions operated during two solar cycle minima are consistent with each other although the magnitude is slightly different. Namely, ρ_{eq} at GEO monotonically increases toward the dusk sector. These variations at GEO have good agreement with previous studies.

[60] 2. The current study extended our understanding of the distribution of ρ_{eq} by including the samples from a wider L range and showed that the magnitude of ρ_{eq} falls logarithmically with increasing L value in the outer magnetosphere while the MLT variations remain consistent with those at GEO.

[61] 3. The current study confirmed that ρ_{eq} at GEO is only weakly correlated with the geomagnetic activities that were represented by the *Kp* and *Dst*. We found that this weak correlation is maintained at other L shells. That is, ρ_{eq} varies little for moderately disturbed times and the short-lived enhancements usually occur during either quiet times or geomagnetic storms.

[62] 4. The current study confirmed the strong correlation of ρ_{eq} with the solar cycle represented by $F_{10.7}$ and the sunspot number, and the empirical model based solely on $F_{10.7}$ may not be enough to represent the solar activity that can ultimately drive density variations.

[63] **Acknowledgments.** We are grateful to Kunihiro Keika for useful discussion. J.B. was supported by NASA grant NNX11AD75G. Work at Dartmouth College and JHUAPL was supported by NSF grant AGS-1105790; R.E.D. was also supported by NASA grant NNX10AQ60G, and K.T. was also supported by NSF grant AGS-1106427. GOES and solar wind data were provided by CDAWeb at NASA GSFC in Greenbelt, Maryland, USA. J.L. was supported by the International Scholarship of Kyung Hee University. The work at Auburn University was supported by NASA grant NNX13AD62G. This work was partly supported by JHU/APL Subcontract No. 937836 to the New Jersey Institute of Technology under NASA Prime Contract No. NAS5-01072.

[64] Masaki Fujimoto thanks the reviewers for their assistance in evaluating this paper.

References

Berube, D., M. B. Moldwin, S. F. Fung, and J. L. Green (2005), A plasmaspheric mass density model and constraints on its heavy ion concentration, *J. Geophys. Res.*, *110*, A04212, doi:10.1029/2004JA010684.

Cummings, W. D., R. J. O'Sullivan, and J. P. J. Coleman (1969), Standing Alfvén waves in the magnetosphere, *J. Geophys. Res.*, *74*, 778–793.

Denton, R. E. (2006), Magneto-seismology using spacecraft observations, in *Magnetospheric ULF Waves: Synthesis and New Directions, Geophysical Monograph Ser.,* vol. 169, edited by K. Takahashi et al., pp. 307–317, AGU, Washington, D. C.

Denton, R. E., M. R. Lessard, R. Anderson, E. G. Miftakhova, and W. J. Hughes (2001), Determining the mass density along magnetic field lines from toroidal eigenfrequencies: Polynomial expansion applied to CRRES data, *J. Geophys. Res.*, *106*(A12), 29,915–29,924, doi:10.1029/2001JA000204.

Denton, R. E., K. Takahashi, R. R. Anderson, and M. P. Wuest (2004a), Magnetospheric toroidal Alfvén wave harmonics and the field line distribution of mass density, *J. Geophys. Res.*, *109*, A06202, doi:10.1029/2003JA010201.

Denton, R. E., J. D. Menietti, J. Goldstein, S. L. Young, and R. R. Anderson (2004b), Electron density in the magnetosphere, *J. Geophys. Res.*, *109*, A09215, doi:10.1029/2003JA010245.

Denton, R. E., K. Takahashi, I. A. Galkin, P. A. Nsumei, X. Huang, B. W. Reinisch, R. R. Anderson, M. K. Sleeper, and W. J. Hughes (2006), Distribution of density along magnetospheric field lines, *J. Geophys. Res.*, *111*, A04213, doi:10.1029/2005JA011414.

Denton, R. E., et al. (2009), Field line distribution of density at L = 4.8 inferred from observations by CLUSTER, *Ann. Geophys.*, *27*(2), 705–724, doi:10.5194/angeo-27-705-2009.

Gallagher, D. L., P. D. Craven, and R. H. Comfort (2000), Global core plasma model, *J. Geophys. Res.*, *105*(A8), 18,819–18,833, doi:10.1029/1999JA000241.

Lemaire, J. F., and K. I. Gringauz (1998), *The Earth's Plasmasphere*, pp. 222–249, Cambridge Univ. Press, New York.

Lennartsson, W. (1989), Energetic (0.1- to 16 keV/e) magnetospheric ion composition at different levels of solar F10.7, *J. Geophys. Res.*, *94*(A4), 3600–3610, doi:10.1029/JA094iA04p03600.

Potemra, T. A., L. J. Zanetti, and M. H. Acuna (1985), The AMPTE CCE magnetic field experiment, *IEEE Trans. Geosci. Remote Sens.*, *GE-23*, 246–249, doi:10.1109/TGRS.1985.289521.

Press, W. H., B. P. Flannery, S. A. Teukolsky, and W. T. Vetterling (1992), *Numerical Recipes*, Cambridge Univ. Press, New York.

Roberts Jr., W. T., J. L. Horwitz, R. H. Comfort, C. R. Chappell, J. H. Waite Jr., and J. L. Green (1987), Heavy ion density enhancements in the outer plasmasphere, *J. Geophys. Res.*, *92*(A12), 13,499–13,512, doi:10.1029/JA092iA12p13499.

Singer, H., L. Matheson, R. Grubb, A. Newman, and D. Bouwer (1996), Monitoring space weather with the GOES magnetometers, in *Society of Photo-Optical Instrumentation Engineers (SPIE) Conference Series.,* vol. 2812, edited by E. R. Washwell, pp. 299–308., Soc. of Photo-Opt. Instrum. Eng., Bellingham, Wash.

Singer, H. J., D. J. Southwood, R. J. Walker, and M. G. Kivelson (1981), Alfvén wave resonances in a realistic magnetospheric magnetic field geometry, *J. Geophys. Res.*, *86*, 4589–4596, doi:10.1029/JA086iA06p04589.

Strangeway, R. J., R. E. Ergun, Y.-J. Su, C. W. Carlson, and R. C. Elphic (2005), Factors controlling ionospheric outflows as observed at intermediate altitudes, *J. Geophys. Res.*, *110*, A03221, doi:10.1029/2004JA010829.

Takahashi, K., and B. J. Anderson (1992), Distribution of ULF energy (f < 80 mHz) in the inner magnetosphere: A statistical analysis of AMPTE CCE magnetic field data, *J. Geophys. Res.*, *97*(A7), 10,751–10,773, doi:10.1029/92JA00328.

Takahashi, K., and R. E. Denton (2007), Magnetospheric seismology using multiharmonic toroidal waves observed at geosynchronous orbit, *J. Geophys. Res.*, *112*, A05204, doi:10.1029/2006JA011709.

Takahashi, K., and B. J. A. R. J. Strangeway (1990), AMPTE CCE observations of Pc3-4 pulsations at L = 2–6, *J. Geophys. Res.*, *95*, 17,179–17,186, doi:10.1029/JA095iA10p17179.

Takahashi, K., R. E. Denton, and D. Gallagher (2002), Toroidal wave frequency at L=6–10: AMPTE/CCE observations and comparison with theoretical model, *J. Geophys. Res.*, *107*, A2, doi:10.1029/2001JA000197.

Takahashi, K., R. E. Denton, R. R. Anderson, and W. J. Hughes (2004), Frequencies of standing Alfvén wave harmonics and their implication for plasma mass distribution along geomagnetic field lines: Statistical analysis of CRRES data, *J. Geophys. Res.*, *109*, A08202, doi:10.1029/2003JA010345.

Takahashi, K., R. E. Denton, R. R. Anderson, and W. J. Hughes (2006), Mass density inferred from toroidal wave frequencies and its comparison to electron density, *J. Geophys. Res.*, *111*, A01201, doi:10.1029/2005JA011286.

Takahashi, K., R. E. Denton, S. Ohtani, W. J. Hughes, and R. R. Anderson (2008), Ion composition in the plasma trough and plasma plume derived from a combined release and radiation effects satellite magnetoseismic study, *J. Geophys. Res.*, *113*, A12203, doi:10.1029/2008JA013248.

Takahashi, K., R. E. Denton, and H. J. Singer (2010), Solar cycle variation of geosynchronous plasma mass density derived from the frequency of standing Alfvén waves, *J. Geophys. Res.*, *115*, A07207, doi:10.1029/2009JA015243.

Tsyganenko, N. A. (1987), Global quantitative models of the geomagnetic field in the cislunar magnetosphere for different disturbance levels, *Planet. Space Sci.*, *35*, 1347–1358, doi:10.1016/0032-0633(87)90046-8.

Tsyganenko, N. A. (1989), A magnetospheric magnetic field model with a warped tail current sheet, *Planet. Space Sci.*, *37*, 5–20, doi:10.1016/0032-0633(89)90066-4.

Ulrich, T. J., and T. N. Bishop (1975), Maximum entropy spectral analysis and autoregressive decomposition, *Rev. Geophys.*, *13*, 183–200.

Vellante, M., U. Villante, M. D. Lauretis, and G. Barchi (1996), Solar cycle variation of the dominant frequencies of Pc3 geomagnetic pulsations at L = 1.6, *Geophys. Res. Lett.*, *12*(23), 1505–1508, doi:10.1029/96GL01399.

Vellante, M., M. Förster, U. Villante, T. L. Zhang, and W. Magnes (2007), Solar activity effect of geomagnetic field line resonance frequencies at low latitudes, *J. Geophys. Res.*, *112*, A02205, doi:10.1029/2006JA011909.

Waters, C. L., F. W. Menk, M. F. Thomsen, C. Foster, and F. R. Fenrich (2006), Remote sensing the magnetosphere using ground-based observation of ULF waves, in *Magnetospheric ULF Waves, AGU Monograph Ser.,* vol. 169, edited by K. Takahashi et al., pp. 319–340, AGU, Washington, D. C.